Sub-Kelvin magnetic and electrical measurements in a diamond anvil cell with

Citation: Palmer, A. et al. "Sub-Kelvin Magnetic and Electrical Measurements in a Diamond Anvil Cell Within Situtunability." Review of Scientific Instruments 86, 9 (September 2015): 093901 © 2015 AIP Publishing LLC

As Published: http://dx.doi.org/10.1063/1.4929861

Publisher: American Institute of Physics (AIP)

Persistent URL: http://hdl.handle.net/1721.1/111958

Version: Final published version: final published article, as it appeared in a journal, conference proceedings, or other formally published context

AIP | Review of Scientific Instruments

Sub-Kelvin magnetic and electrical measurements in a diamond anvil cell with in situ tunability

A. Palmer, D. M. Silevitch, Yejun Feng, Yishu Wang, R. Jaramillo, A. Banerjee, Y. Ren, and T. F. Rosenbaum

Citation: Review of Scientific Instruments **86**, 093901 (2015); doi: 10.1063/1.4929861
View online: http://dx.doi.org/10.1063/1.4929861
View Table of Contents: http://scitation.aip.org/content/aip/journal/rsi/86/9?ver=pdfcov
Published by the AIP Publishing

Sub-Kelvin magnetic and electrical measurements in a diamond anvil cell with *in situ* tunability

A. Palmer,[1] D. M. Silevitch,[1] Yejun Feng,[1,2] Yishu Wang,[1] R. Jaramillo,[3] A. Banerjee,[4] Y. Ren,[2] and T. F. Rosenbaum[1,5]
[1]*The James Franck Institute and Department of Physics, The University of Chicago, Chicago, Illinois 60637, USA*
[2]*The Advanced Photon Source, Argonne National Laboratory, Argonne, Illinois 60439, USA*
[3]*Department of Materials Science and Engineering, Massachusetts Institute of Technology, Cambridge, Massachusetts 02138, USA*
[4]*Quantum Condensed Matter Division, Oak Ridge National Laboratory, Oak Ridge, Tennessee 37831, USA*
[5]*Division of Physics, Mathematics, and Astronomy, California Institute of Technology, Pasadena, California 91125, USA*

(Received 29 June 2015; accepted 19 August 2015; published online 4 September 2015)

We discuss techniques for performing continuous measurements across a wide range of pressure–field–temperature phase space, combining the milli-Kelvin temperatures of a helium dilution refrigerator with the giga-Pascal pressures of a diamond anvil cell and the Tesla magnetic fields of a superconducting magnet. With a view towards minimizing remnant magnetic fields and background magnetic susceptibility, we characterize high-strength superalloy materials for the pressure cell assembly, which allows high fidelity measurements of low-field phenomena such as superconductivity below 100 mK at pressures above 10 GPa. *In situ* tunability and measurement of the pressure permit experiments over a wide range of pressure, while at the same time making possible precise steps across abrupt phase transitions such as those from insulator to metal. © *2015 AIP Publishing LLC*. [http://dx.doi.org/10.1063/1.4929861]

I. INTRODUCTION

When materials change state, they provide insights into their fundamental nature. Reaching a phase transition may require the application of large external fields, yet the region of experimental interest is often confined to a small region in a multi-dimensional phase space. Examples of recent interest in condensed matter and quantum physics include nematic electronic order in H-T space,[1] exotic superconductivity of heavy fermions in P-T space,[2] quantum critical points in H-P-T space,[3] and competing charge-density wave (CDW) and superconducting ground states in P-x-T-H space,[4] where H is magnetic field, P is pressure, T is temperature, and x is composition. In general, such studies require precise control and accurate measurement of the sample environment, compatible with the measurement technique of choice.

Hydrostatic pressure is a particularly powerful tuning parameter, as it offers the possibility of substantially varying interaction strengths without introducing either disorder from doping or a symmetry-breaking field. Combined with suitable experimental probes, it is a valuable tool for studying approaches to quantum phase transitions and associated critical behavior.[2,4,5] High pressure measurements at cryogenic temperatures of 4 K and below have been performed using a wide range of experimental techniques, including electrical transport,[4–10] magnetic susceptibility,[7,9,11] Shubnikov-de Haas and de Haas-van Alphen quantum oscillations,[12,13] infrared and Raman spectroscopy,[14,15] and neutron and x-ray magnetic diffraction.[10,16–19] Pressure-driven experiments at temperatures below 1 K (Refs. 4, 6, 9, and 20) entail the use of cryostats such as recirculating helium-3 (Ref. 21) or helium dilution refrigerators. Successfully integrating high-pressure cells into such cryostats is a challenging task.

For piston cylinder cells, Bridgman anvil cells,[9] and large volume multi-anvil presses,[8,21] the pressurization process often requires several tons of external force and has to take place at room temperature. Such cells usually do not provide optical access for secondary pressure calibration using spectroscopic methods, requiring the cryogenic pressure to be estimated from the applied force load or measured from a manometer such as the superconducting transition temperature in lead or the structural transition temperature of bismuth. Thus, changing the pressure requires a time consuming thermal cycle, and it can be difficult to both precisely set and precisely measure the pressure. On the other hand, diamond anvil cells (DACs) require much less force (maximum ~10 kN = 1 ton) to operate,[22] which is in a range accessible to low-temperature gas-driven actuators.[23] They are also compatible with optical access for *in situ* pressure measurement[24–26] and provide a much broader pressure range than large volume vessel cells. Recently, we have demonstrated that DACs can maintain a high-quality pressure environment with homogeneity and isotropy comparable to large-volume cells,[11,26,27] a key requirement for studying condensed matter phenomena.

Here, we adapt DACs for use at sub-Kelvin temperatures in a helium dilution refrigerator, including continuous tuning and *in situ* pressure monitoring capability. Cryogenic force applicators based on helium gas-driven bellows and membrane actuators have a long history[28] and have been successfully used to drive high-pressure diamond anvil cells.[11,23,26,29–31] Such an actuator allows a nearly continuous pressure change; equally important, it saves significant time and effort by eliminating

the need to thermally cycle to room temperature.[11,23,26,29] *In situ* pressure tuning becomes substantially more powerful when paired with a fast and accurate technique for pressure measurement, such as ruby fluorescence[25,26] or diamond Raman spectroscopy.[24] Both the helium gas actuator and the optical path for fluorescence need to be constructed with the constraints of sub-Kelvin cryostats in mind. In particular, minimizing the heat load and thermal conductivity of these systems is crucial in light of the hundred microwatt scale cooling power of typical helium dilution refrigerators. This has been the main obstacle for integrating other versatile high-pressure systems with a milli-Kelvin environment[21] and was not discussed in the previous installations in dilution refrigerators.[23]

An additional challenge in performing high-pressure measurements in the sub-Kelvin regime is that the low temperature represents an energy scale that is typically accompanied by a similarly low magnetic field scale, and thus it is often necessary to reduce the background field to 10 Oe or below. This necessitates constructing the pressure cell and sample chamber from materials that are both non-ferromagnetic and of high mechanical strength. Here, we focus on the choice of gasket material, as the gasket has the closest spatial proximity to the samples in the pressure chamber. While BeCu has been used in sub-Kelvin measurements,[23] stronger materials are highly desirable in order to sustain a large and stable pressure chamber.[26] We discuss here the suitability of Cr-rich Ni-based superalloys as gasket materials for magnetic measurements at the lowest temperatures.

The development of instruments for probing *H*-*P*-*T* phase space in the sub-Kelvin region extends our previous development at higher temperatures.[11] We illustrate the capabilities of our apparatus using two examples: tracking the evolution of an elemental superconductor down to 30 mK over 11 GPa of pressure, and measuring a pressure-driven insulator-metal transition below 85 mK.

II. OPERATION OF *IN SITU* TUNED DAC IN A HELIUM DILUTION REFRIGERATOR

The overall assembly scheme of our apparatus is shown in Fig. 1(a). At the center is the diamond anvil cell containing the sample. The cell is attached to the cold finger of a helium dilution refrigerator, placing the sample at the field center of an 8/10 T superconducting magnet. The bore of the solenoid magnet has a 3 in. diameter, allowing the use of a pressure cell with a ~2 in. diameter while still leaving clearance for a vacuum can and a still-plate-mounted radiation shield. The DAC is based on the 3-pin Merrill-Bassett design, similar to that of Ref. 23. It allows for a gas-driven actuator with a contact area of 12-18 cm^2, enough to drive the DAC to the limit of its strength using the 2200 psi range of a standard helium gas bottle. For more compact superconducting magnets, a 1-in. diameter bellows-driven diamond anvil cell with *in situ* ruby manometer[11] can be substituted, with the limitation that the smaller actuator provides ~5 kN of force at 2200 psi helium gas pressure, about half of the 10 kN force needed to tune the DAC over its entire pressure range.[22] If necessary, the remaining half of the force could be provided by spring washers during room-temperature assembly.

The *in situ* control of cell pressure is driven by helium gas from a room-temperature manifold introduced via a stainless steel capillary line (0.50 mm ID, 0.80 mm OD) to a disk-shaped or toroidal actuator that exerts force on the cell. To thermalize the room temperature helium gas, the steel capillary tubing is first wound around oxygen-free high conductivity (OFHC) copper bobbins and then silver soldered to the bobbins under tension for good thermal contact. The bobbins are screwed to anchoring points at several thermal stages of the dilution refrigerator: vacuum can flange (4.2 K), condenser (2 K), still (600 mK), cold plate (60 mK), and mixing chamber (lowest $T < 30$ mK under load). A minimum of 50 cm of coiled tubing separates each stage to minimize the thermal conductivity between the different stages of the refrigerator.

In operation, consideration must be given to the phase diagram of helium-4. Below 365 psi, ^{4}He is in either a gaseous or superfluid phase for all temperatures[32] and thus can flow freely inside the capillary line to transmit pressure. However, the large thermal conductivity of superfluid helium limits the base temperature of our dilution refrigerator to approximately 50 mK. The superfluid region of the helium phase diagram can be avoided entirely through the suitable choice of diamond anvil size and initial sealing pressure of the DAC. At temperatures below 2.2 K and pressure above 365 psi, helium is in a solid phase.[32] The base temperature of our fridge with solid helium in the actuator and capillary line was 28 mK, not significantly different than the base temperature with the actuator and capillary line under vacuum. In this actuator pressure regime, adjusting the cell pressure must be performed above the helium melting temperature to ensure that there are no solid helium blockages inside the capillary line. In wet fridges, this is most easily performed by stopping the circulation and condenser pumps, and introducing small amounts of helium exchange gas into the inner vacuum space to bring the system to 4.2 K. In dry systems, stopping the circulation and using heaters to raise the temperatures has a similar effect. It should be noted that systems which have the capillary line pass directly through a liquid helium bath are limited to a maximum actuator pressure of 14 MPa (2030 psi), the solidification pressure of helium at 4.2 K. Upon cooling, the helium freezing in the capillary line typically results in a 1%-3% drop of the total cell pressure.

Pressure measurements use standard ruby fluorescence.[25,26] A 532 nm laser beam is attenuated to 100-3000 μW depending on the sample temperature range and coupled into the cryostat using a 400 μm diameter multimode optical fiber. To reduce the coupling of 300 K blackbody radiation into the sample space, an IR-blocking absorptive short-pass filter (KG2, Schott, Inc.) with 83% transmissivity at 700 nm is placed in-line with the fiber and anchored to the 4 K stage of the dilution refrigerator. The same fiber provides the pathway to collect the 695-700 nm ruby fluorescence response. The pressure was calculated using the 4.5 K calibration curve reported in Ref. 26.

With the cell mounted at field center of the superconducting magnet, the coupling between the fiber and the sample chamber is accomplished via a pair of BK7 spherical plano-convex lenses integrated into an OFHC copper cold finger connected to the cryostat mixing chamber (Fig. 1(b)). The use of large (1 in. diameter) spherical lenses gives the optical

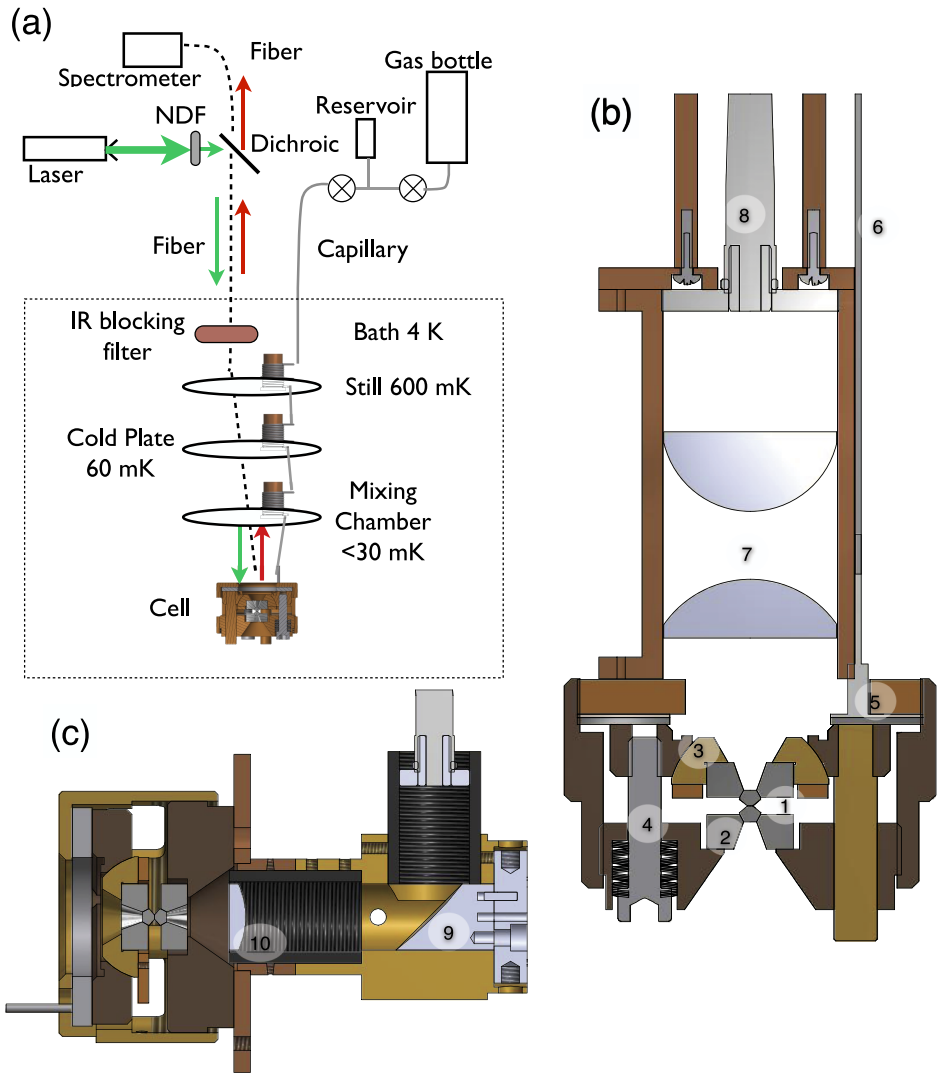

FIG. 1. Diamond anvil cell assembly mounted on a helium dilution refrigerator. (a) Overall layout of the assembly. For pressure measurements, 532 nm laser light is attenuated by a neutral-density filter (NDF), fiber-coupled into the refrigerator, and focused on the sample chamber of the DAC. Ruby fluorescence (~695 nm) is coupled back through the same fiber and measured by a spectrometer. An infrared-blocking filter at 4 K blocks room-temperature blackbody radiation. Pressure is tuned by pressurizing a thin membrane with helium from a room-temperature manifold. A capillary line, thermally anchored to copper bobbins at each temperature stage, connects the manifold to the membrane. (b) Pressure cell and optics mounted at the end of a cold finger for in-field measurements: (1) Diamond anvils. (2) Non-magnetic sapphire or silicon nitride seats. (3) Alignment rocker. (4) Brass compression screws with BeCu Belleville spring washers used for initial sealing and pressurization at room temperature. (5) 316L stainless steel helium membrane. (6) Capillary line. (7) Plano-convex coupling lenses. (8) 400 μm multimode optical fiber. (c) Cell and optics mounted directly to the mixing chamber for zero-field measurements: (9) Truncated-parabola mirror. (10) Plano-convex focusing lens.

system sufficient depth of field and coupling efficiency that thermal contractions between room temperature and 4 K do not significantly degrade the overall efficiency. For experiments that do not require an external magnetic field, the thermal linkage between the cell and the cryostat can be improved by directly clamping the cell to the mixing chamber of the refrigerator (Fig. 1(c)). In this geometry, optical coupling between the fiber and the cryostat can be realized by a truncated-parabola mirror and a spherical focusing lens.

With the laser beam attenuated to 100 μW and a corresponding increase in the spectrometer integration time to 30-60 s per measurement, the cell pressure can be tracked continuously from several Kelvins down to approximately 200 mK with minimal impact on dilution refrigerator performance. It would be straightforward to extend this measurement to lower T with additional attenuation and integration, although in practice the cell pressure was found to remain highly stable below 2 K. The cell pressure was recorded before and after sample measurements; the laser was shuttered while the samples were measured to avoid possible direct heating of the sample from even a heavily attenuated laser beam.

III. HIGH STRENGTH, NON-MAGNETIC MATERIALS AT SUB-KELVIN TEMPERATURES

The study of magnetism and superconductivity at sub-Kelvin temperatures may require a sample environment free from spurious fields. Superconducting elements with a T_c below 1 K typically have a critical field H_c below 100 Oe,[33] with the critical field becoming only a few Oe for materials with critical temperatures below 0.1 K. To study materials with such temperature and field scales at high pressure, cells must

be built from materials that have both sufficient strength and are free of ferromagnetic or superconducting behavior deep into the milli-Kelvin regime. This puts stringent constraints on suitable cell and gasket materials.[34] Our pressure cell is built from non-magnetic silicon aluminum bronze (C64200),[11] and the seats to support diamond anvils are made of either silicon nitride or sapphire. Tungsten carbide seats are not suitable because cobalt is commonly used as a binder material.

The choice of gasket material for use below 1 K is crucial. Rhenium, a standard option at higher temperatures, superconducts below 1.7 K at ambient conditions and up to 3 K when strained[35] and hence strongly perturbs susceptibility measurements. BeCu can be magnetic due to trace impurities.[36] In addition, the precipitation hardening mechanism, Be accumulation at Cu grain boundaries, deteriorates under pressure as the gasket deforms and new grain boundaries form. Therefore, instead of work hardening, BeCu gaskets grow weaker with increasing pressure, which results in noticeable sample deformation.[23] By contrast, alloys that exhibit significant work-hardening are a fruitful source for potential gasket materials. For iron-based stainless steel materials, pure iron in the ferrite (BCC, α) phase and Fe_3C in the martensite (body center tetragonal) phase are both ferromagnetic, while Fe in the austenite (FCC, γ) and the hexaferrum (HCP, ε) phases are not.[37] Nevertheless, the nominally austenitic 300 series stainless steels are often ferromagnetic at 4 K due to trace impurities, thermal cycling, or welding.[38] With the possible exception of 316LN,[38] commonly available 300 series stainless steels are not ideal gasket choices for sub-Kelvin high-pressure magnetic measurements that are sensitive to fields of several Oe.

We look instead for high-strength, non-magnetic materials among the nickel and cobalt based superalloys. Similar to stainless steels, superalloys consist of a dominant component from the Ni-Co-Fe group, a minor component from the Cr-Mo-W group, and traces of other elements. They are designed for superb mechanical strength for applications at high load condition and high temperature, such as turbine engine blades in jet airplanes and boiler linings in coal-fired power stations.[39] Here, we focus on superalloys in the wrought condition, instead of cast single-crystal types,[39] as the wrought alloys are more widely available and economical, and are better suited for the deformation seen in high pressure cell gaskets. Superalloys in the wrought condition are typically strengthened by three methods. Solid solution annealing dissolves elements such as Mo and W into the Ni or Co matrix to increase stiffness from an enhanced Debye temperature, but the strengthening method is typically only effective at temperatures above 1000 °C. Mechanical cold working creates numerous dislocation centers that strengthen the material. Finally, in multi-phase alloys, age hardening creates precipitants of either carbides (M_6C or $M_{23}C_6$, with M = Cr, Ni, Mo, W, Ta, Nb) or intermetallics (A_3B type with A = Ni, Co, and B = Ti, Al, Ta) in the grain boundaries.

These superalloys have been deployed at cryogenic temperatures, including applications in outer space exploration,[40] high-field magnets,[41,42] and high-pressure vessels.[34] However, the cryogenic magnetic properties of these superalloys are not well understood. Among the parent ferromagnetic elements, Ni has the smallest magnetic moment per atom at 0.60 μ_B, compared to 1.7 μ_B and 2.2 μ_B for Co and Fe, respectively, suggesting that a Ni-based superalloy should provide a relatively low magnetic susceptibility. In $Ni_{1-x}Cr_x$, the Curie temperature T_c is linearly suppressed with increasing Cr content, going to zero at x = 13 at. %.[43] $Ni_{1-x}Cr_x$ is continuously miscible in the FCC phase only up to x = 22 at. % (~20 wt. %) Cr before forming an ordered Ni_2Cr phase.[43] In the Inconel 600 series, increasing the Cr concentration from 0 to 20 wt. % suppresses T_c from 750 K to 92 K.[40,44] Adding Mo and W increases the miscibility limit to 36 at. % Cr/Mo/W (Table I), suggesting that one should look for non-magnetic materials in Ni dominated superalloys with a high Cr-Mo-W concentration. This is exemplified by Inconel 625, MP35N, and Hastelloy C276, all of which have high Cr/Mo/W concentrations. The first two are known to be paramagnets at 6 K and 4.2 K, respectively, while Hastelloy C276 is a spin glass at 3 K.[34,40,42]

To explore suitable superalloys as pressure-cell components in low temperature magnetism and superconductivity experiments, we procured five specimens from commercial suppliers. Their compositions are listed in Table I, sorted by calculated Cr-Mo-W concentration from 26 to 36 at. %. The materials were chosen because of their high mechanical strengths under cold-working and thermal aging conditions. Hastelloy C22HS (Haynes International), Inconel 686, and Udimet L605 (Special Metals Co) were provided in solution-annealed temper. Elgiloy (Elgiloy Specialty Metals) was provided in age-hardened temper after cold-rolling. Cold-rolled MP35N was provided in 0.25 mm shim form (Hamilton Precision Metals). The Udimet L605, Inconel 686, and Hastelloy C22HS were further cold worked with a 50%+ reduction in thickness using a hydraulic press. Age hardening of cold-worked C22HS and MP35N was performed at elevated temperatures in air for 24 h at 605 °C, and 4 h at 565 °C, respectively, and subsequently air quenched. Another widely

TABLE I. Compositions of five tested superalloys. wt. % was specified by either the manufacturer or electron microprobe measurement. Minor trace elements are not listed.

	Components (wt. %)								
Alloy name	Co	Ni	Fe	Cr	Mo	W	Total Co/Ni/Fe (at. %)	Total Cr/Mo/W (at. %)	FCC phase volume (%)
Elgiloy	39.45	15.27	15.9	19.6	7.14	0	70.5	26.2	~90
Udimet L-605	51.15	10.82	2.55	21.56	0.04	13.88	69.1	30.9	~90
MP35N	33.13	36.52	0.05	20.02	10.15	0	70.7	29.3	100
Hastelloy C22HS	0.11	61.23	1.14	20.89	16.63	0	64.9	35.1	99.9
Inconel 686	0	59.31	0.18	20.3	15.9	4.0	63.7	36.3	100

used Ni-based superalloy is 40HNU-VI, commonly known as Russian Alloy,[34] and subsequently reinvented at a limited scale in Japan.[45] We obtained a piece of 40HNU-VI of Russian origin and in the wrought condition.

We examined the structural properties of the six superalloys under various work and thermal histories using high-energy x-ray powder diffraction with a two-dimensional area detector. The measurement was carried out at beam line 11-ID-C of the Advanced Photon Source using 111.052 keV x-rays at 295 K (Fig. 2). Even with a significant density of dislocation centers, our measurements found that many superalloys remained in a single FCC phase, including Inconel 686 and MP35N under various cold work and heat treatment conditions. Hastelloy C22HS is also predominantly in the FCC phase, although precipitation hardening forms $Ni_2(Mo, Cr)$ particles as large as 10 nm in extensively precipitated (~1000 h) specimens.[46] We found only a trace presence of $Ni_2(Mo, Cr)$ with a volume ratio less than 0.1% (Fig. 2) for a heat treatment time of 24 h. Udimet L605 and Elgiloy both showed a significant volume (~10%) of minor phases in addition to the FCC majority phase. Alloy 40HNU-VI is mainly composed of Ni, Cr, and Al, and the significant amount (3-4 wt. %) of Al causes a relatively large volume of cubic-structured Ni_3Al that is present in the wrought condition. The large concentration of Cr (~40 wt. %) caused phase separation, characterized by an electron microprobe as Cr-rich and Ni-rich regions of at least 2 μm size. All three phases in 40HNU-VI were observed clearly via x-ray diffraction study (Fig. 2). We note that Ni_3Al can be weakly ferromagnetic with a strong dependence on stoichiometry[47] and size.[48]

We measured the magnetization of these alloys using a SQUID magnetometer (Magnetic Properties Measurement System, Quantum Design) for fields between ±5 T at temperatures from 3.5 to 5 K (Fig. 3). There is a clear inverse correlation between susceptibility $\chi = \frac{dM}{dH}\Big|_{H=0}$ and Ni concentration. Elgiloy and Udimet L605 have the lowest Ni and Cr/Mo/W concentrations among the five alloys and the largest susceptibilities. Inconel 686 and Hastelloy C22HS have large Ni fractions and also the largest Cr/Mo/W concentration, and hence the smallest susceptibilities. MP35N is between these two limits. No ferromagnetic hysteresis was observed in any of the materials in this temperature range.

We chose MP35N and C22HS to investigate more completely as pressure-cell gasket materials due to their combination of strength, uniform structural phases, and relatively low susceptibilities. We plot in Fig. 4 the magnetic susceptibility $\chi'(T)$ of MP35N and C22HS for $0.065 \le T \le 25$ K and $0.080 \le T \le 25$ K, respectively. Instead of

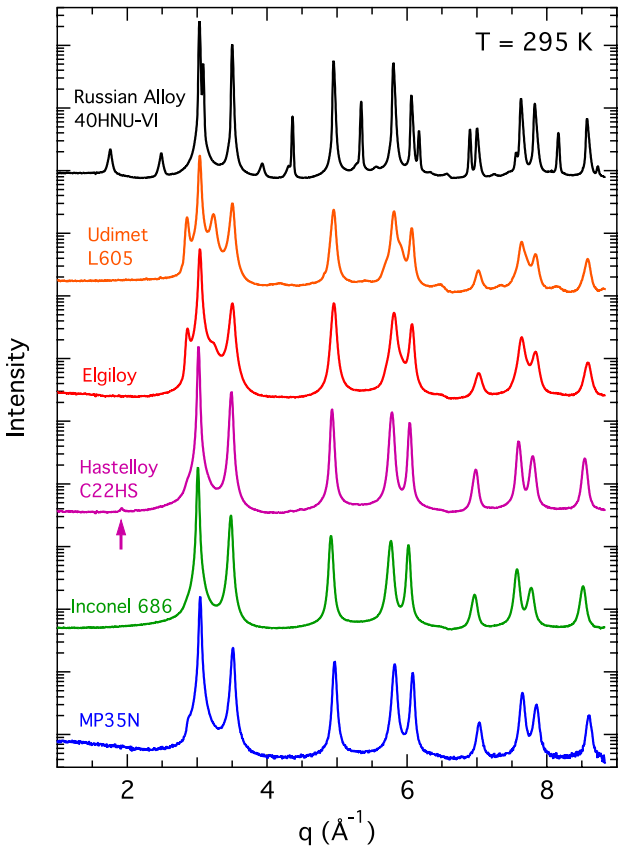

FIG. 2. X-ray powder diffraction patterns of six superalloys. Curves are shifted vertically for clarity and are displayed in sequence of decreasing structural complexity (top to bottom). Russian alloy 40HNU-VI is in a wrought form; the other five alloys have been cold worked. Elgiloy, Hastelloy C22HS, and MP35N have been thermally hardened. MP35N and Inconel 686 are both in a single FCC structural phase, while Hastelloy C22HS shows a minor phase at our detection sensitivity limit. The intensity of the diffraction peak marked by the arrow corresponds to a volume ratio of approximately 0.1%.

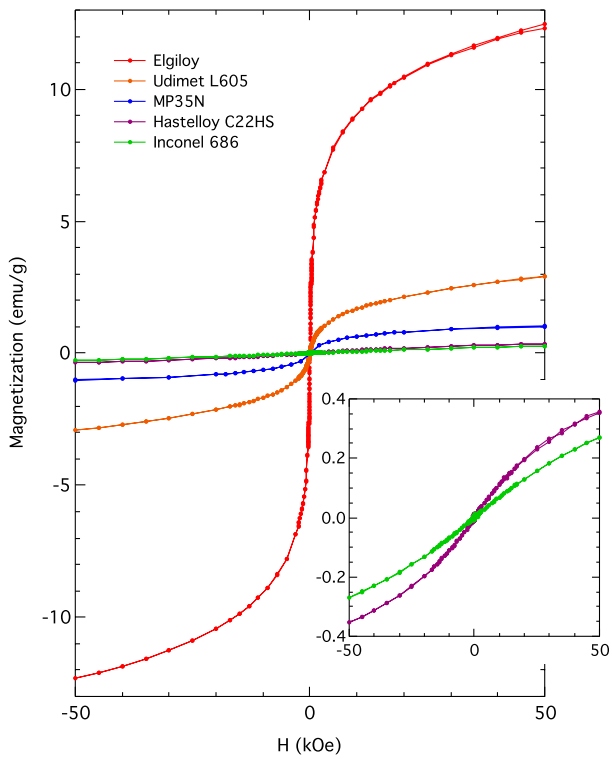

FIG. 3. Magnetization $M(H)$ curves of the Ni/Co/Fe superalloys listed in Table I measured by SQUID magnetometry at $T = 3.5$ K (Elgiloy), 4.0 K (MP35N), and 5.0 K (Hastelloy C22HS, Udimet L605, Inconel 686). Inconel 686 was measured in the annealed temper. Despite the large concentration of ferromagnetic Ni, Co, and Fe, no hysteresis was observed. By comparison, pure Fe and Ni have saturation magnetizations of 221.7 emu/g and 58.6 emu/g, respectively, and Hastelloy C276 has a saturation magnetization of 3.0 emu/g,[42] comparable to Udimet L605 reported here. Magnetic susceptibility χ', measured by the slope of $M(H)$ in the $H = 0$ limit, varies over four decades from $1.68 \cdot 10^{-2}$ emu/(g Oe) for Elgiloy to $7.23 \cdot 10^{-6}$ emu/(g Oe) for Inconel 686.

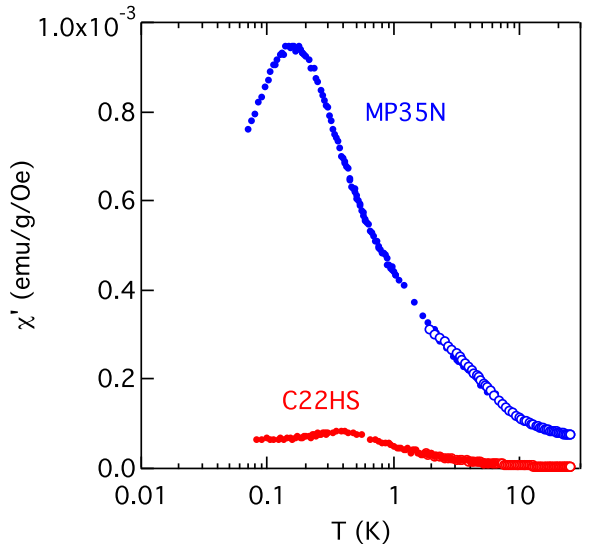

FIG. 4. Magnetic susceptibility $\chi'(T)$ of MP35N and age-hardened C22HS. Open circles: SQUID magnetometry measured in a MPMS magnetometer from above 10 K to 1.8 K in 100 Oe field. The maximum susceptibility of C22HS is approximately 10× smaller than that of MP35N. Solid circles: ac susceptibility, measured with a 0.1 Oe/167 Hz drive field from 6 K to below 100 mK in the dilution refrigerator. Rounded peaks at 160 mK (MP35N) and 380 mK (C22HS) suggest the onset of spin-glass states rather than ferromagnetic ordering.

the diverging susceptibility with decreasing T characteristic of ferromagnetic ordering, MP35N and C22HS both have rounded low temperature peaks in χ'(T). They are found for these materials at 160 mK and 380 mK, respectively, suggesting the onset of a spin glass state. Here, MP35N and C22HS clearly manifest the desired outcomes from the principles deduced above: preserve a single phase FCC lattice structure with a large Ni component and minimal amount of Fe and Co, and suppress the itinerant ferromagnetism with a high concentration of Cr/Mo/W. The glassy behavior likely arises from the disorder associated with the Ni/Co/Fe composition.

IV. MILLI-KELVIN SUPERCONDUCTING TRANSITIONS UNDER PRESSURE

As noted above, superconductivity in the milli-Kelvin regime typically is accompanied by characteristic field scales well below 100 Oe. Here, we demonstrate the low magnetic background and broad pressure range of our system by measuring the pressure evolution of the critical temperature and field of iridium. Ir is a type-I superconductor with T_c = 112 mK and H_{c1} = 16 Oe at ambient pressure.[49] At P = 1.1 GPa, T_c is suppressed by approximately 6%.[50] Here, we examine both T_c and H_c in iridium as a function of pressure up to 11.0 GPa.

Annealed polycrystalline iridium foil (Goodfellow, 99.9%) was polished to a thickness of 30 μm using an Al_2O_3 suspension. A 240 × 170 μm^2 sample was diced using a razor blade. Pressure was applied using two Drukker-type diamonds with 800 μm culets. The gasket was made from 250 μm thick MP35N shim stock pre-indented to a thickness of 130 μm before thermal hardening. A hole of 430 μm diameter was electrical discharge machined for the sample chamber. The Ir sample was sealed under pressure together with a ruby manometer in a 4:1 methanol:ethanol mixture pressure medium. The magnetic behavior was probed using an ac susceptibility technique with the coils surrounding the diamonds at a frequency of 167 Hz and a drive field of 0.1 Oe, in both the amplitude- and frequency-independent limits.[11] The output signal was measured with a transformer pre-amplifier and a lock-in analyzer (SR554 and SR830, Stanford Research Systems, Inc., respectively). The background at 4 K was nulled by an adjustable compensation coil, mounted external to the cryostat.[11] Background nulling also can be achieved using the offset/expand functionality common to digital lock-in amplifiers. However, using an external nulling circuit allows the amplifier to be run at higher analog gain and use the full dynamic range of its analog-to-digital converter, resulting in better noise performance.

We show in Fig. 5(a) the susceptibility as a function of dc field, $\chi'(H)$, at T = 30 mK. This is the most efficient and straightforward way to detect the transition for

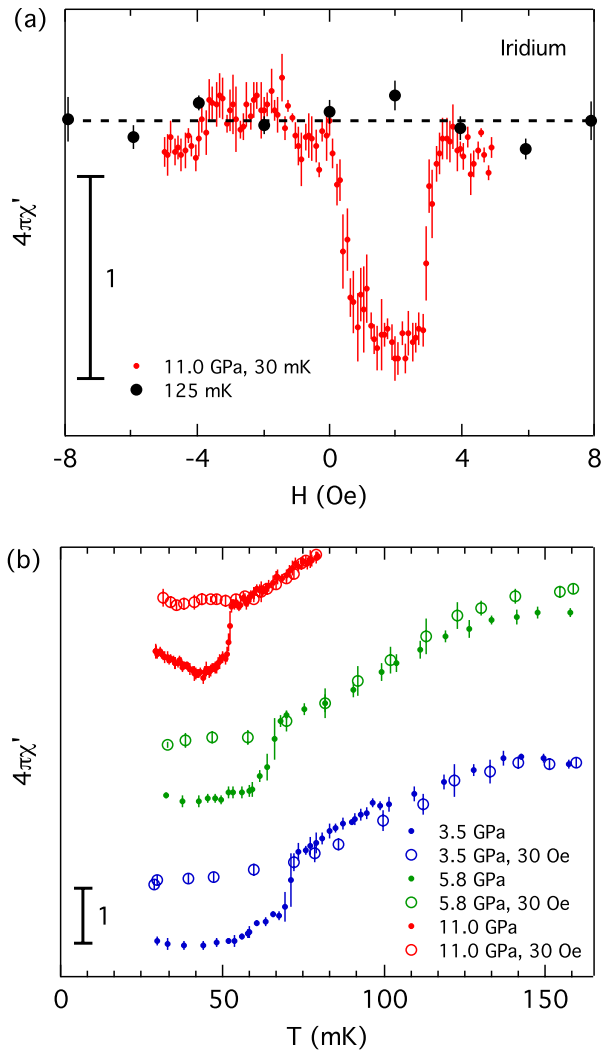

FIG. 5. Superconductivity under pressure in iridium. (a) Susceptibility $\chi'(H)$ at 11 GPa for T = 30 and 125 mK, below and above the zero-field T_c. The 30 mK data show a field offset of 1.7 Oe, indicating the presence of a constant, axial DC field. (b) Susceptibility vs. temperature for a series of pressures (solid circles), showing the Meissner effect at the superconducting transition. Applying a 30 Oe field quenches the superconductivity at each pressure (open circles).

superconducting materials with a low critical field H_{c1}.[51] We note that the zero field position is shifted by 1.7 Oe in Fig. 5(a), indicating the presence of a small remnant field from components of the DAC. The corresponding Fig. 5(b) presents the temperature evolution of $\chi'(T)$ for the superconducting transition in iridium at pressures 3.5 GPa, 5.8 GPa, and 11.0 GPa. The data compare $\chi'(H)$ at (the compensated) $H = 0$ and at 30 Oe, where the superconductivity is suppressed. The temperature scans were taken with discrete steps of 0.5-10 mK size and integrated for 1000 s at each temperature step. These discrete temperature steps allow for both thermal equilibration and statistical integration. The transition width at 11.0 GPa is 1.5 mK, indicating a high degree of pressure homogeneity across the sample.

We did not observe the superconducting transition in Ir beyond 13 GPa, presumably because the critical field H_{c1} at $T = 30$ mK became less than the combination of the Earth's magnetic field (~0.5 Oe) and the remnant magnetic field due to various parts of the DAC. We summarize in Fig. 6 the pressure evolution of both T_c and H_{c1} of iridium, with ambient-pressure measurements of H_{c1} (Ref. 49) shown for comparison. High permeability shields could be added outside or inside the cryostat to further reduce the stray field environment.[51]

V. GROOVED GASKET FOR ELECTRICAL TRANSPORT MEASUREMENTS IN DIAMOND ANVIL CELLS

High-pressure electrical transport measurements, including resistivity and Hall effect, provide a macroscopic measurement of itinerant charge behavior in the H-P-T phase space.[4,5,10,52] The key challenge associated with such measurements is the task of feeding delicate electrical leads into the pressure chamber without electrical shorts or breaks.[8,9,53] For diamond anvil cells, in particular, this challenge is complicated by the use of metallic gaskets to form the pressure chamber.

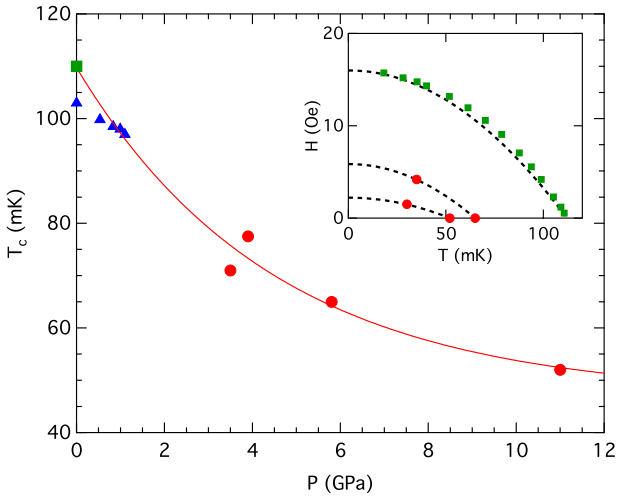

FIG. 6. Superconducting transition temperature T_c as a function of pressure for iridium. Our measured results (red circles) are compared with ambient pressure value (green square) from Ref. 49 and low pressure values (blue triangles) from Ref. 50. (Inset) $H_{c1}(T)$ values of Ir for ambient pressure (green squares, values from Ref. 49), 5.8 GPa, and 11.0 GPa (red circles). Dashed lines show calculated $H_{c1}(T)$ curves assuming an isotropic gap.

The use of such malleable gaskets was a key development for providing a homogeneous and stable pressure environment.[54] This stability is of particular importance for dilution refrigerator experiments where the time, effort, and cost required to cycle to room temperature to replace a failed cell are large compared to higher temperature cryostats.

One common solution to this challenge employs an underlying metallic gasket coated with a suitable insulating layer, typically a mixture of Al_2O_3 powder and binding epoxy.[6,27] Such a composite gasket largely preserves the continuous malleability and mechanical stability of a purely metallic gasket, while insulating the sample's electrical leads. However, gaskets are most stable when the amount of metallic surface area in contact with both diamond anvils is maximized. In addition, deformation of the composite gasket during pressurization can result in cracking or flaking of the coating on the inner wall of the sample chamber.[27] This may result in either electrical shorts of the sample leads to the metallic portion of the gasket or to pressure inhomogeneities as epoxy intrudes into the pressure chamber. Here, we follow the alternative approach of grooved composite gaskets[53,55,56] and discuss an improved design to increase the reliability of the process.

The motivation behind the grooved gasket approach is to create insulating channels in the gasket only underneath the electrical leads, thereby leaving the majority of the gasket surface area metallic to maximize the stability of the cell. This technique was originally developed for Bridgman pressure vessels.[53] Previous use of the grooving technique in diamond anvil cells placed the grooves and coating on one side of the gasket for 4-wire measurements of bar-shaped samples.[55,56] This asymmetry in construction potentially can cause an imbalance in a cell's response to pressurization. Instead, we use here a cross pattern for grooving. In addition to improved stability from the more symmetric arrangement, the cross patterned grooves are compatible with samples in the van der Pauw measurement geometry, enabling the measurement of Hall coefficients under pressure[5,10] along with the longitudinal resistivity.

We outline in Fig. 7 the grooved gasket preparation procedure. A pilot hole, less than half the diameter of the final sample chamber, is drilled in shim stock using either a microdrill press or wire electrical discharge machining. The shim is pre-indented on the DAC to a thickness roughly halfway between the shim thickness and final target thickness of the gasket. To create the channels in the gasket, two pieces of tungsten wire with a diameter of 50-100 μm are taped in a cross geometry over the pilot hole. A smaller diameter tungsten wire maximizes the amount of metallic surface area, but increases the difficulty of positioning sample wires in the groove. This assembly is re-indented in the DAC to the final desired thickness. The tungsten wires are pressed into the metallic gasket, creating the lead channels. For gasket materials that need heat-treatment (e.g., MP35N), this grooving process needs to be carried out before the thermal hardening process. The excess tungsten at the intersection of the wires is pressed into the pilot hole, reducing the localized stress in the center of the diamond anvil. The tungsten wires can be removed once fully indented, normally by pulling them from the metallic gasket using tweezers. If the ends of the tungsten wires are sheared

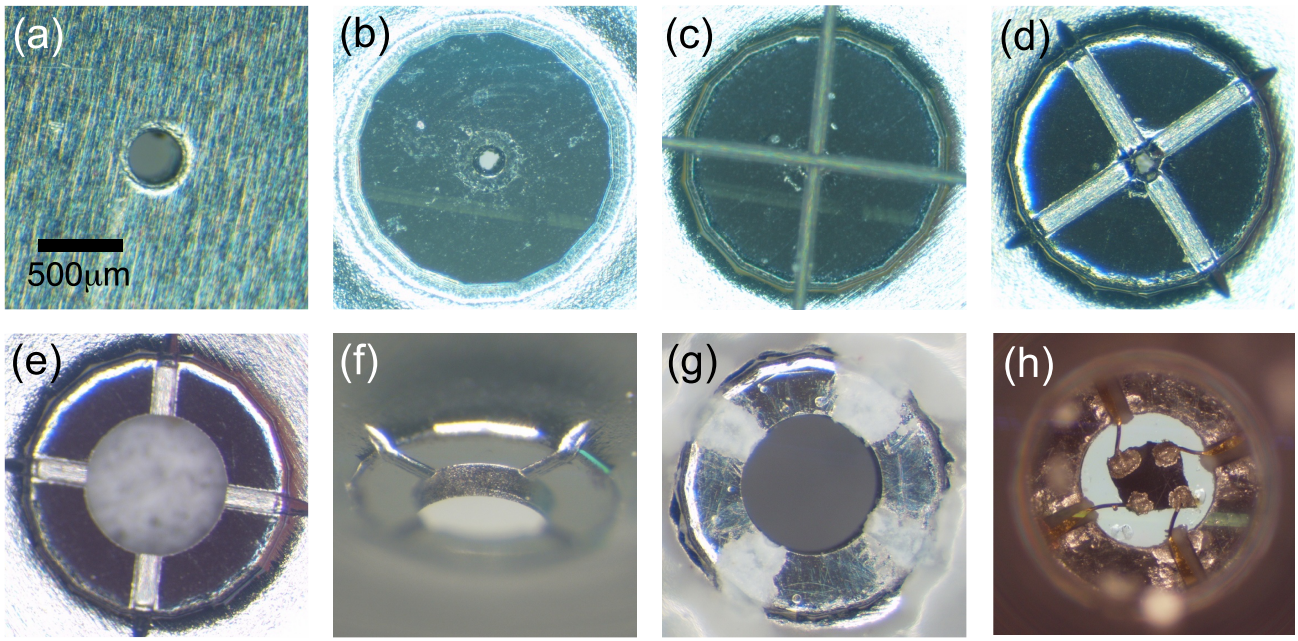

FIG. 7. Images of various stages in grooved gasket preparation for electric transport measurements, shown here for 1.5 mm culet diamonds and a SS316 gasket. (a) Pilot hole drilled in gasket shim stock. (b) Pre-indentation of gasket to 150% target thickness, while keeping the pilot hole in the middle of the diamond culet. (c) Tungsten wires are placed in a cross pattern over the pilot hole and held with tape (outside of view). (d) Gasket with tungsten wires is indented to the final desired thickness, and then the wires are removed. The tungsten wires are pressed into the gasket material to create grooves. (e) Sample chamber is drilled using an electron discharge machine or laser. (f) The groove depth is approximately 20%-25% of the gasket thickness and has a clean profile. (g) Grooves are coated with an insulating mixture of Al_2O_3 powder and UV-curing epoxy. (h) Sealed pressure chamber with sample placed in the chamber and conducting leads over the insulating grooves. In this assembly, a compatible conductive epoxy (EPO-TEK377, Epoxy Technology) and a Methanol:Ethanol 4:1 pressure medium were used.

off, the tungsten can be removed by re-drilling the pilot hole from the other side of the gasket. The sample chamber is drilled to the final diameter using either an electrical discharge machine or a laser to eliminate burring, and the gasket is heat treated if necessary. A 4:1 mixture of Al_2O_3 and NOA81 UV-curing epoxy (Norland Products) is applied to the channels and gasket surfaces external to the sample chamber,[27] and the coating is cured 40 cm from a 175 W mercury-vapor UV lamp for 30 min. The gasket is then indented a third time to flatten the epoxy layer. The sample is positioned with leads on top of the insulating channels during DAC loading. This "ceramic epoxy" becomes transparent upon pressurization.

When a highly compressible liquid pressure medium is used, some of the insulating epoxy can be pushed into the sample chamber during the initial sealing process (Fig. 7(h)), carrying the leads along with it. The extruded leads typically push on the sample asymmetrically, causing it to rotate (Fig. 7(h) and Ref. 27). This effect becomes more severe with small sample chambers, potentially leading to sample rotation of more than 90°, and hence the risk of shorting electrical contacts to each other. Small sample chambers are also at greater risk of becoming crowded with extruded epoxy, which can degrade the hydrostaticity condition or damage the sample. Thus, the sample chamber diameter should be as large as possible, consistent with stability under pressure. Our sample chambers typically are 50%-55% of the diameter of the diamond culet. Care must be taken to assure a round, well-centered sample chamber. The diameter of tungsten wire used is less sensitive to changes in diamond size. For diamonds with culets of 1.5 mm, tungsten wires with diameters larger than 75 μm can be used to ease sample positioning without significantly affecting the ratio of metal to epoxy surface area. For diamond culets smaller than 1 mm, a smaller diameter of 50 μm for the tungsten wire is desirable.

VI. PRESSURE DRIVEN INSULATOR-METAL TRANSITION IN THE ZERO-TEMPERATURE LIMIT

NiS_2 is a canonical charge-transfer Mott insulator.[57,58] At zero temperature, NiS_2 can be driven from an insulator to a metal using applied pressure[58,59] or doping.[58,60] We measure the resistivity of NiS_2 as a function of pressure across the insulator-metal transition at $T < 100$ mK. This effort demonstrates the precise control of *in situ* pressure tuning necessary for studies of quantum phase transitions in the $T \to 0$ limit.

NiS_2 samples were prepared by cleaving and polishing single crystals to a thickness of 40 μm, followed by razor-blade dicing to 200 μm × 200 μm lateral size. The sample surface was etch cleaned using 4% by volume ammonium sulfide $(NH_4)_2S$ for 2 h. Four 25 μm Au leads were attached in a van der Pauw geometry using conductive silver epoxy (LCA-24, Bacon Industries), and loaded into a DAC with 1.5 mm culet diamonds and a gasket prepared with a fully insulated surface.[27] LCA-24 epoxy dissolves in a 4:1 methanol:ethanol mixture, so a 1:1 mixture of n-pentane:isopentane was used instead as a pressure medium.[61] The resistivity of the sample was measured using a pair of SR830 lock-in amplifiers in the insulating regime and a LR-700 ac resistance bridge in the metallic regime.

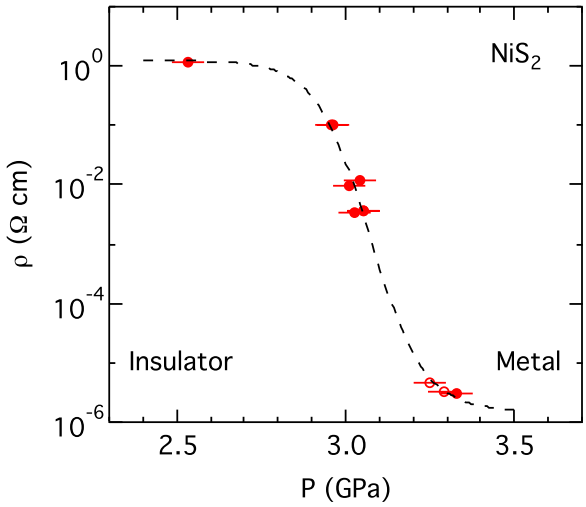

FIG. 8. Pressure driven insulator-metal transition in NiS_2 at 45 mK $< T <$ 85 mK (solid symbols) and extrapolated (<0.5% in ρ) from 580 mK in the metal (open symbols). Line is a guide to the eye.

We plot in Fig. 8 the resistivity of NiS_2 as a function of pressure for temperatures between 45 and 85 mK. The insulator-metal transition is clearly visible as the resistivity of the sample drops by over 5 orders of magnitude in a narrow range of 0.8 GPa. The transition pressure P_c was 3.0 ± 0.1 GPa, consistent with the transition pressure for the disappearance of the antiferromagnetic superlattice peak (1/2, 1/2, 1/2) probed by x-ray diffraction.[62]

VII. CONCLUSIONS

We describe in detail an experimental setup for performing electrical transport and magnetic susceptibility measurements across *P-T-H* space, suitable for characterizing both classical and quantum phase transitions. The selection of materials for the DAC construction is an important factor in positioning experiments for success. We focus on the choice of gasket materials because the gasket's structural and magnetic properties are essential to being able to characterize superconductors and magnets at milli-Kelvin temperatures. We describe as well a more reliable approach to gasket preparation for measurements of both the diagonal and off-diagonal components of the electrical conductivity.

The helium-driven membrane structure, installed to vary pressure *in situ* at low temperature, provides both a wide range of accessible pressures and fine-tuning capability with a precision of 0.05 GPa. We demonstrate the broad dynamic range through measurements of the superconducting transition in elemental iridium and precise resolution when examining the narrow pressure range of the insulator-metal transition in NiS_2. The DAC and associated optics can be mounted in the bore of a superconducting magnet, permitting additional tuning by tesla magnetic fields. The optical access provided by the broadband fiber coupling provides not only *in situ* pressure calibration using ruby fluorescence techniques but also opens the possibility of probes such as Raman scattering and optical pumping under pressure at dilution refrigerator temperatures.

ACKNOWLEDGMENTS

We thank V. Struzhkin for providing the 40HNU-VI alloy sample for testing, J. M. Honig for growing the NiS_2 samples, S. Sinogeikin at HP-CAT (Sector 16) of the Advanced Photon Source for development of helium diaphragm membranes, and J. S. Schilling for useful conversations. The work at the University of Chicago was supported by the National Science Foundation (Grant No. DMR-1206519) and used MRSEC shared facilities (NSF Grant No. DMR-1420709). D.M.S. acknowledges support from the U.S. Department of Energy Office of Basic Energy Sciences (Grant No. DE-FG02-99ER45789). The work at the Advanced Photon Source of Argonne National Laboratory was supported by the U.S. Department of Energy Basic Energy Sciences under Contract No. DE-AC02-06CH11357. SQUID magnetometry measurements were performed in part at the Center for Nanoscale Materials, a U.S. Department of Energy Office of Science User Facility, under Contract No. DE-AC02-06CH11357 with the assistance of B. Fisher.

[1]R. A. Borzi, S. A. Grigera, J. Farrell, R. S. Perry, S. J. S. Lister, S. L. Lee, D. A. Tennant, Y. Maeno, and A. P. Mackenzie, Science **315**, 214 (2007).
[2]P. Monthoux, D. Pines, and G. G. Lonzarich, Nature **450**, 1177 (2007).
[3]S. E. Rowley, L. J. Spalek, R. P. Smith, M. P. M. Dean, M. Itoh, J. F. Scott, G. G. Lonzarich, and S. S. Saxena, Nat. Phys. **10**, 367 (2014).
[4]A. F. Kusmartseva, B. Sipos, H. Berger, L. Forró, and E. Tutiš, Phys. Rev. Lett. **103**, 236401 (2009).
[5]R. Jaramillo, Y. Feng, J. Wang, and T. F. Rosenbaum, Proc. Natl. Acad. Sci. U. S. A. **107**, 13631 (2010).
[6]K. Shimizu, T. Yamauchi, N. Tamitani, N. Takeshita, M. Ishizuka, K. Amaya, and S. Endo, J. Supercond. **7**, 921 (1994).
[7]M. Debessai, T. Matsuoka, J. J. Hamlin, J. S. Schilling, and K. Shimizu, Phys. Rev. Lett. **102**, 197002 (2009).
[8]J. G. Cheng, K. Matsubayashi, S. Nagasaki, A. Hisada, T. Hirayama, M. Hedo, H. Kagi, and Y. Uwatoko, Rev. Sci. Instrum. **85**, 093907 (2014).
[9]G. Giriat, Z. Ren, P. Pedrazzini, and D. Jaccard, Solid State Commun. **209-210**, 55 (2015).
[10]Y. Feng, A. Palmer, Y. Wang, D. M. Silevitch, and T. F. Rosenbaum, Phys. Rev. B **91**, 155142 (2015).
[11]Y. Feng, D. M. Silevitch, and T. F. Rosenbaum, Rev. Sci. Instrum. **85**, 033901 (2014).
[12]S. Araki, R. Settai, M. Nakashima, H. Shishido, S. Ikeda, H. Nakawaki, Y. Haga, N. Tateiwa, T. C. Kobayashi, H. Harima, H. Yamagami, Y. Aoki, T. Namiki, H. Sato, and Y. Onuki, J. Phys. Chem. Solids **63**, 1133 (2002).
[13]C. Martin, C. C. Agosta, S. W. Tozer, H. A. Radovan, T. Kinoshota, and M. Tokumoto, J. Low Temp. Phys. **138**, 1025 (2005).
[14]I. F. Silvera and R. J. Wijngaarden, Phys. Rev. Lett. **47**, 39 (1981).
[15]S.-I. Kimura and H. Okamura, J. Phys. Soc. Jpn. **82**, 021004 (2012).
[16]I. Mirebeau, I. N. Goncharenko, P. Cadavez-Peres, S. T. Bramwell, M. J. P. Gingras, and J. S. Gardner, Nature **420**, 54 (2002).
[17]Y. Feng, R. Jaramillo, G. Srajer, J. C. Lang, Z. Islam, M. S. Somayazulu, O. G. Shpyrko, J. J. Pluth, H. K. Mao, E. D. Isaacs, G. Aeppli, and T. F. Rosenbaum, Phys. Rev. Lett. **99**, 137201 (2007).
[18]J. Wang, Y. Feng, R. Jaramillo, J. van Wezel, P. C. Canfield, and T. F. Rosenbaum, Phys. Rev. B **86**, 014422 (2012).
[19]Y. Feng, J. Wang, A. Palmer, J. A. Aguiar, B. Mihaila, J.-Q. Yan, P. B. Littlewood, and T. F. Rosenbaum, Nat. Commun. **5**, 4218 (2014).
[20]M. I. Eremets, K. Shimizu, T. C. Kobayashi, and K. Amaya, Science **281**, 1333 (1998).
[21]K. Matsubayashi, A. Hisada, T. Kawae, and Y. Uwatoko, Rev. High Pressure Sci. Technol. **22**, 206 (2012).
[22]D. J. Dunstan and I. L. Spain, J. Phys. E: Sci. Instrum. **22**, 913 (1989).
[23]A. W. Webb, D. G. Gubser, and L. C. Towle, Rev. Sci. Instrum. **47**, 59 (1976).
[24]Y. Akahama and H. Kawamura, J. Appl. Phys. **100**, 043516 (2006).
[25]K. Syassen, High Pressure Res. **28**, 75 (2008).
[26]Y. Feng, R. Jaramillo, J. Wang, Y. Ren, and T. F. Rosenbaum, Rev. Sci. Instrum. **81**, 041301 (2010).

[27]R. Jaramillo, Y. Feng, and T. F. Rosenbaum, Rev. Sci. Instrum. **83**, 103902 (2012).
[28]J. H. R. Ward, Rev. Sci. Instrum. **36**, 1376 (1965).
[29]G. A. N. Connell, J. A. Wilson, and A. D. Yoffe, J. Phys. Chem. Solids **30**, 287 (1969).
[30]R. Letoullec, J. P. Pinceaux, and P. Loubeyre, High Pressure Res. **1**, 77 (1988).
[31]J. C. Chervin, B. Canny, J. M. Besson, and P. Pruzan, Rev. Sci. Instrum. **66**, 2595 (1995).
[32]I. L. Spain and S. Segall, Cryogenics **11**, 26 (1971).
[33]N. Ashcroft and N. D. Mermin, *Solid State Physics* (Cengage Learning, Belmont, 1976).
[34]I. R. Walker, Rev. Sci. Instrum. **70**, 3402 (1999).
[35]C. Chu, T. Smith, and W. Gardner, Phys. Rev. Lett. **20**, 198 (1968).
[36]B. A. Jordan, J. Mater. Sci. **4**, 1097 (1969).
[37]S. S. Saxena and P. B. Littlewood, Nature **412**, 290 (2001).
[38]K. Pieterman, A. Ketting, and J. C. Geerse, J. Phys. Colloq. **45**, 625 (1984).
[39]R. C. Reed, *The Superalloys: Fundamentals and Applications* (Cambridge University Press, Cambridge, 2008).
[40]I. B. Goldberg, M. R. Mitchell, A. R. Murphy, R. B. Goldfarb, and R. J. Loughran, Adv. Cryog. Eng. Mater. **36**, 755 (1990).
[41]F. M. G. Wong and N. A. Mitchell, Adv. Cryog. Eng. Mater. **44**, 65 (1998).
[42]J. Lu, E. S. Choi, and H. D. Zhou, J. Appl. Phys. **103**, 064908 (2008).
[43]P. Nash, Bull. Alloy Phase Diagrams **7**, 466 (1986).
[44]Y. Okada, K. Yoshikawa, and T. Yukitoshi, J. Jpn. Inst. Met. **45**, 496 (1981), https://www.jstage.jst.go.jp/article/jinstmet1952/45/5/45_5_496/_article.
[45]Y. Uwatoko, S. Todo, K. Ueda, A. Uchida, M. Kosaka, N. Mori, and T. Matsumoto, J. Phys.: Condens. Matter **14**, 11291 (2002).
[46]X. Xie, Y. Zeng, L. Kou, J. Dong, L. M. Pike, and D. Klarstrom, *Superalloys 2008* (The Minerals, Metals, and Materials Society, 2008), p. 799.
[47]F. R. de Boer, C. J. Schinkel, J. Biesterbos, and S. Proost, J. Appl. Phys. **40**, 1049 (1969).
[48]D. Mukherji, R. Müller, R. Gilles, P. Strunz, J. Rösler, and G. Kostorz, Nanotechnology **15**, 648 (2004).
[49]D. G. Gubser and R. J. Soulen, Jr., J. Low Temp. Phys. **13**, 211 (1973).
[50]W. Wejgaard, Phys. Lett. A **29**, 396 (1969).
[51]J. Tuoriniemi, K. Juntunen-Nurmilaukas, J. Uusvuori, E. Pentti, A. Salmela, and A. Sebedash, Nature **447**, 187 (2007).
[52]R. P. Smith, M. Sutherland, G. G. Lonzarich, S. S. Saxena, N. Kimura, S. Takashima, M. Nohara, and H. Takagi, Nature **455**, 1220 (2008).
[53]J. S. Schilling, Adv. Phys. **28**, 657 (1979).
[54]W. A. Bassett, High Pressure Res. **29**, 163 (2009).
[55]T. Adachi, H. Tanaka, H. Kobayashi, and T. Miyazaki, Rev. Sci. Instrum. **72**, 2358 (2001).
[56]H. Cui, Y. Okano, B. Zhou, A. Kobayashi, and H. Kobayashi, J. Am. Chem. Soc. **130**, 3738 (2008).
[57]N. F. Mott and Z. Zinamon, Rep. Prog. Phys. **33**, 881 (1970).
[58]J. A. Wilson and G. D. Pitt, Philos. Mag. **23**, 1297 (1971).
[59]N. Takeshita, S. Takashima, C. Terakura, H. Nishikubo, S. Miyasaka, M. Nohara, Y. Tokura, and H. Takagi, e-print arXiv:cond-mat/0704.0591 (2007).
[60]X. Yao, J. M. Honig, T. Hogan, C. Kannewurf, and J. Spałek, Phys. Rev. B **54**, 17469 (1996).
[61]S. Klotz, J. C. Chervin, P. Munsch, and G. Le Marchand, J. Phys. D: Appl. Phys. **42**, 075413 (2009).
[62]Y. Feng, R. Jaramillo, A. Banerjee, J. M. Honig, and T. F. Rosenbaum, Phys. Rev. B **83**, 035106 (2011).